Earthquake Fault Rupture Modeling and Ground-Motion Simulations for the Southwest Iceland Transform Zone Using CyberShake

Otilio Rojas*[1], Marisol Monterrubio-Velasco[1], Juan E. Rodríguez[1], Scott Callaghan[2], Claudia Abril[1,3], Benedikt Halldorsson[4,5], Milad Kowsari[4,5], Farnaz Bayat[5], Kim B. Olsen[6], Alice-Agnes Gabriel[3,7], and Josep de la Puente[1]

ABSTRACT

CyberShake is a high-performance computing workflow for kinematic fault-rupture and earthquake ground-motion simulation developed by the Statewide California Earthquake Center to facilitate physics-based probabilistic seismic hazard assessment (PSHA). CyberShake exploits seismic reciprocity for wave propagation by computing strain green tensors along fault planes, which in turn are convolved with rupture models to generate surface seismograms. Combined with a faultwide hypocentral variation of each simulated rupture, this procedure allows for generating ground-motion synthetics that account for realistic source variability. This study validates the platform's kinematic modeling of physics-based seismic wave propagation simulations in Southwest Iceland as the first step toward migrating CyberShake from its original study region in California. Specifically, we have implemented CyberShake workflows to model 2103 fault ruptures and simulate the corresponding two horizontal components of ground-motion velocity on a 5 km grid of 625 stations in Southwest Iceland. A 500-yr-long earthquake rupture forecast consisting of 223 hypothetical finite-fault sources of M_w 5–7 was generated using a physics-based model of the bookshelf fault system of the Southwest Iceland transform zone. For each station, every reciprocal simulation uses 0–1 Hz Gaussian point sources polarized along two horizontal grid directions. Comparison of the results in the form of rotation-invariant synthetic pseudoacceleration spectral response values at 3, 4, and 5 s periods are in good agreement with the Icelandic strong motion data set and a suite of empirical Bayesian ground-motion prediction equations (GMPEs). The vast majority of the physics-based simulations fall within one standard deviation of the mean GMPE predictions, previously estimated for the area. At large magnitudes for which no data exist in Iceland, the synthetic data set may play an important role in constraining GMPEs for future applications. Our results comprise the first step toward comprehensive and physics-based PSHA for Southwest Iceland.

KEY POINTS

- We perform physics-based earthquake fault rupture modeling in the Southwest Iceland transform zone based on a 500-year earthquake rupture forecast.
- The physics-based ground-motion simulations carried out using CyberShake are consistent with a suite of ground-motion prediction equations (GMPEs) for the region.
- At large magnitudes, the CyberShake results may help constrain GMPEs for future applications.

Supplemental Material

INTRODUCTION

Iceland is the most seismically active region in northern Europe. It is a volcanic island in the North Atlantic Ocean

1. Barcelona Supercomputing Center (BSC-CNS), Barcelona, Spain, https://orcid.org/0000-0002-2852-8101 (OR); https://orcid.org/0000-0003-0790-1832 (MM-V); https://orcid.org/0000-0002-4715-2154 (JER); https://orcid.org/0000-0002-3365-8613 (CA); https://orcid.org/0000-0003-2608-1526 (JP); 2. Statewide California Earthquake Center, University of Southern California, Los Angeles, California, U.S.A., https://orcid.org/0000-0001-5992-6025 (SC); 3. Ludwig-Maximilians University, Munich, Germany, https://orcid.org/0000-0003-0112-8412 (A-AG); 4. Icelandic Meteorological Office, Reykjavik, Iceland, https://orcid.org/0000-0001-5591-8757 (BH); https://orcid.org/0000-0002-4331-4021 (MK); 5. University of Iceland, Reykjavík, Iceland; 6. San Diego State University, San Diego, California, U.S.A., https://orcid.org/0000-0002-3078-485X (KBO); 7. Institute of Geophysics and Planetary Physics, Scripps Institution of Oceanography, University of California at San Diego, La Jolla, California, U.S.A.

*Corresponding author: otilio.rojas@bsc.es

Cite this article as Rojas, O., M. Monterrubio-Velasco, J. E. Rodríguez, S. Callaghan, C. Abril, B. Halldorsson, M. Kowsari, F. Bayat, K. B. Olsen, A.-A. Gabriel, *et al.* (2024). Earthquake Fault Rupture Modeling and Ground-Motion Simulations for the Southwest Iceland Transform Zone Using CyberShake, *Bull. Seismol. Soc. Am.* **115**, 69–85, doi: 10.1785/0120240064

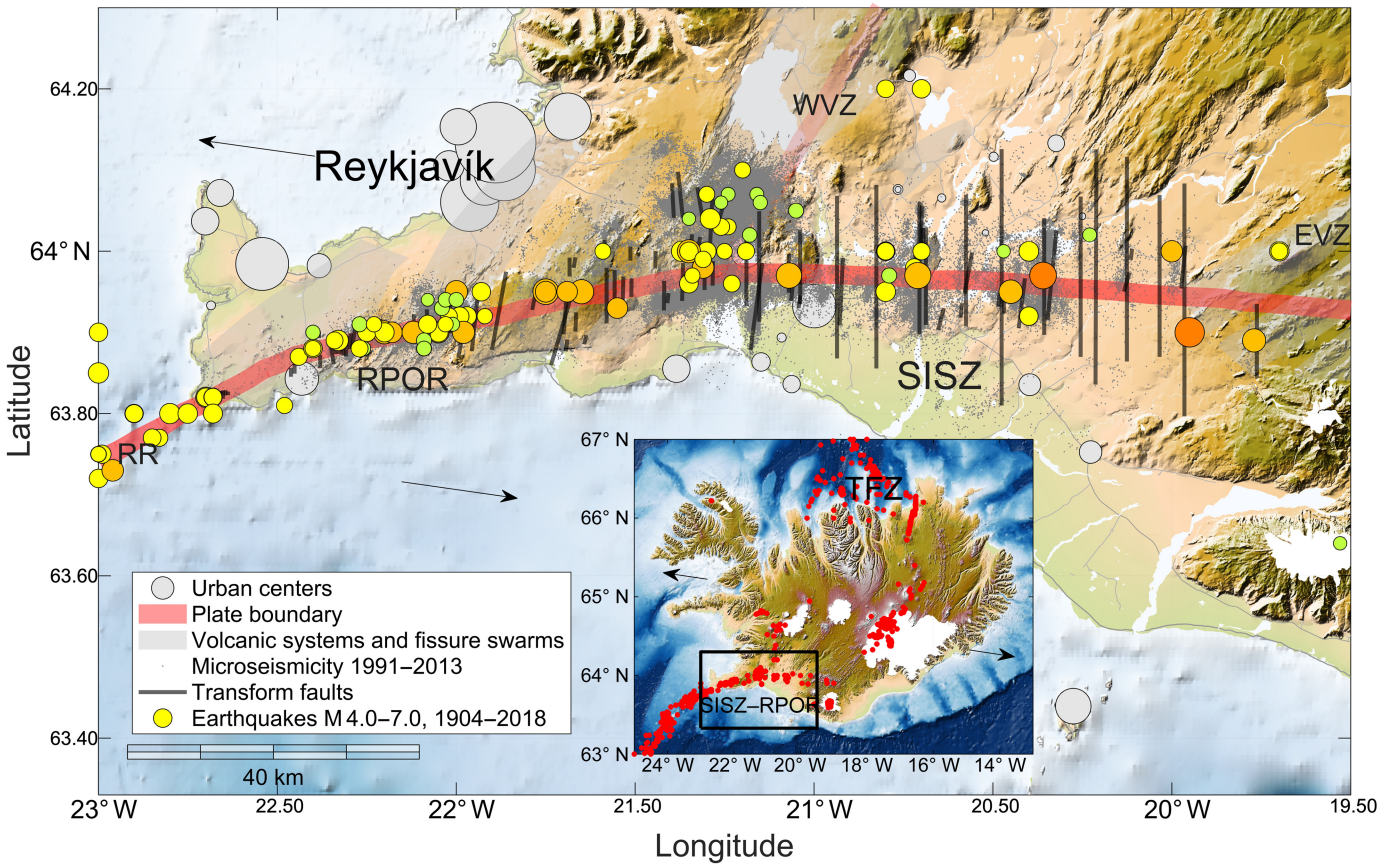

and is the areal part of a massive flood-basalt plain produced by the Icelandic Hot Spot, a vertical magmatic thermal anomaly under central Iceland (Tryggvason *et al.*, 1983; Thordarson and Hoskuldsson, 2002). There it coincides with the Mid-Atlantic Ridge (MAR), the extensional plate boundary between the North American and Eurasian plates. The interplay of the MAR and the Hot Spot drives the volcanic and seismic activity of Iceland (Fig. 1). Spatially, its seismic activity follows the present-day axis of active tectonic extension of the MAR in Iceland: it approaches from southwest where the subaerial Reykjanes ridge (RR) becomes aerial and joins the Reykjanes Peninsula oblique rift (RPOR), continues east through the South Iceland seismic zone (SISZ), turns north along the eastern volcanic zone, northern volcanic zone (NVZ), and back toward west via the complex and largely subaerial Tjörnes fracture zone (TFZ). On the western edge of the TFZ, the MAR continues north of Central Iceland.

The eastward ridge jump of the extensional plate boundary in Iceland has resulted in the formation of two significant transform zones: the complex and extensive TFZ mostly offshore North Iceland, and the Southwest Iceland transform zone, comprising the SISZ and the RPOR. Historically, the largest earthquakes in Iceland of $M_w \sim 7$ have repeatedly taken place in these transform zones according to historical annals of ~1000 yr, teleseismic recordings of ~100 yr, and the last ~30 yr of local recordings of seismic strong motions (Tryggvason *et al.*, 1958; Einarsson, 1991, 2008, 2014; Stefansson *et al.*, 2008; Sigbjörnsson *et al.*, 2014; Einarsson *et al.*, 2020; Steigerwald *et al.*, 2020; Jónasson *et al.*, 2021). As a result, the SISZ–RPOR is one of two regions in Iceland where the seismic hazard is highest. In addition, the SISZ–RPOR is completely aerial and much more densely populated than the TFZ. Despite the RPOR mostly being a barren elevated plateau of basaltic Holocene lava shields, it contains several coastal towns most notable of which is the capital region of Reykjavik where approximately two-thirds of the national population lives. Farther east and collocated with

Figure 1. The Southwest Iceland transform zone, consisting of the South Iceland seismic zone (SISZ) in the South Iceland lowlands and the Reykjanes Peninsula oblique rift zone (RPOR). The red line denotes the centerline of the plate boundary across southwest Iceland with vectors denoting the approximate direction of transcurrent motion across the SISZ–RPOR. The instrumental microseismic catalog from 1991 to 2013 is shown as dots (minimum magnitude of 0, with 1 being the magnitude of completeness), and significant earthquakes from 1904 to 2019 (Jónasson *et al.*, 2021) of the ICEL–NMAR catalog as circles, spanning magnitudes from M_w 4 (green circles) to 7 (dark orange circles). The black lines denote the mapped and inferred locations of dextral strike-slip faults of the bookshelf fault system. Distinct volcanic systems in volcanic zones (see acronyms in the Introduction) are oriented northeast–southwest and shown as gray-shaded regions. The inset map shows Iceland, an island in the North Atlantic Ocean, along with significant earthquakes from 1904 to 2019 (red dots), the locations of the two transform zones (see text in the Introduction), and arrows indicating the direction of tectonic plate spreading. The boundary of the larger map of southwest Iceland is shown by the black rectangle. The color version of this figure is available only in the electronic edition.

the SISZ lies the South Iceland lowland, the country's largest agricultural region. The SISZ–RPOR contains typical infrastructure pertinent to modern society and its lifelines such as electric power transmission lines, hydroelectric and geothermal power plants, dams, bridges, roads, and pipelines.

A reliable estimation of seismic risk benefits from a reliable probabilistic seismic hazard assessment (PSHA). The current seismic hazard map for Southwest Iceland was published in 2010, but more importantly, it needs a comprehensive revision as several recent research findings have shown (for an overview see, e.g., Kowsari *et al.*, 2021, 2022). Namely, it has conclusively been shown that the fault system in Southern Iceland, previously thought to be confined to the SISZ region continues toward the west and all along the RPOR (Einarsson *et al.*, 2020; Steigerwald *et al.*, 2020). In addition, the maximum seismogenic potential of the SISZ-RPOR, and in particular in the RPOR is seen to decrease systematically from east to west (see in Bayat *et al.*, 2022). That necessitates a subdivision of the Southwest Iceland transform zone into subzones, each of which having a specific maximum earthquake magnitude and a specific earthquake magnitude–frequency distribution (MFD). However, the most recent compilation of a harmonized instrumental earthquake catalog of significant earthquakes in Iceland since 1900 (Jónasson *et al.*, 2021) is too sparse along the transform zone (see Fig. 1), in particular for the RPOR, to allow the derivation of reliable subzone MFDs. This is of practical importance as the central and eastern RPOR fault system lies near the capital region of Iceland.

Fortunately, the above limitations have effectively been addressed through the development of a physics-based earthquake fault system model of the Southwest Iceland transform zone. The rate of tectonic transform motion across the zone (Sigmundsson *et al.*, 1995; Hreinsdóttir *et al.*, 2001; Árnadóttir *et al.*, 2006; Sigmundsson, 2006) along with the fault system geometry have been used to calibrate the fault system model that also captures the variation of seismogenic depth along the transform zone (Bayat *et al.*, 2022). The model allows random realizations of the fault system configuration where each causative fault is completely specified by its dimensions, maximum potential seismic magnitude, and long-term slip rate, along with uncertainty estimates, effectively composing an earthquake rupture forecast (ERF). It also allows the derivation of subzone-specific MFDs, the cumulative seismic activity of which is not only consistent with, but effectively explains, the earthquake catalog of the Southwest Iceland transform zone (Bayat *et al.*, 2024). In particular, the ability of the model to generate realizations of long-term finite-fault earthquake catalogs (Kowsari *et al.*, 2022) means that it lends itself particularly useful for a physics-based Monte Carlo stochastic approach to PSHA, that is, earthquake rupture modeling and seismic ground-motion simulation using the kinematic modeling approach. Not only is a Monte Carlo approach to PSHA a more physically realistic approach, but it also enables better incorporation of uncertainties into the PSHA estimates (see, e.g., Sigbjörnsson *et al.*, 1995; Atkinson, 2012; Kowsari *et al.*, 2023). The underlying hypothesis is to assume that the seismogenesis of each fault follows a certain probabilistic model of seismicity (e.g., Poissonian, Markovian), and parameterization for which depends on pre-existing data and models. The Monte Carlo approach to PSHA has been used since 1995 in Iceland (Sigbjörnsson *et al.*, 1995; Solnes *et al.*, 2004) but more recently in various regions of the world for which various seismicity models apply (Atkinson, 2012; Bayraktar *et al.*, 2017; Karaca, 2021).

Computational seismology using high-performance computing (HPC) has explored physical models to explain the mechanisms that govern earthquake rupture and seismic wave propagation. When modeling earthquake ruptures, kinematic models prescribe finite-slip evolution in space and time and allow exploration of the variability of seismic moment, fault orientation, hypocenter location, source time function, and rupture path. Dynamic rupture models, on the other hand, use the physics of rock failure to model how earthquakes start, dynamically propagate, and arrest on a particular fault geometry, and may furthermore explore differences in fault frictional parameters, coseismic multifault interaction, and local stress distributions (e.g., Li *et al.*, 2023). The sampling of source parameters and their variability combined with the simulation of wave propagation accounting for wave-physics effects have allowed a physics-based approach to PSHA (Frankel *et al.*, 2007; Graves *et al.*, 2011; Bradley *et al.*, 2018; Callaghan *et al.*, 2021; Milner *et al.*, 2021). The computational platform for such a calculation needs to efficiently simulate the ground motions at each site for a large (at least in the order of thousands) ensemble of rupture variations. For instance, Graves *et al.* (2011) and Callaghan *et al.* (2021) assembled an ERF by compiling the likely source variability on California fault systems, consistent with slip inversions of past earthquakes (Field *et al.*, 2009). Alternatively, Milner *et al.* (2021) used a rate-and-state earthquake simulator RSQSim to simulate hundreds of thousands of years of synthetic seismicity, also in California. This source variability allows complementing earthquake catalogs with synthetic data of moderate- and large-magnitude ranges making them suitable for potential PSHA studies.

CyberShake integrates the Graves–Pitarka (GP) pseudodynamic fault-rupture generator with an anelastic wave propagation solver for ground-motion simulation, being originally developed to undertake PSHA studies in southern California (Graves *et al.*, 2011; Silva *et al.*, 2016; Jordan and Callaghan, 2018). This computational workflow has benefitted from a significant evolution in HPC facilities for efficient simulation of hundreds of thousands of events. These simulations are carried out in reciprocal mode. For every hazard location, two simulations are performed, each one using a surface delta function polarized along a horizontal direction to compute the response of the strain tensor at each fault surface point (strain green tensors [SGT]). SGT time histories require a significant disk storage amount, on the order of 1–2 TB per hazard site

(Maechling *et al.*, 2007; Callaghan *et al.*, 2015), according to the total number of fault segments on the ERF database. The convolution of these SGTs with numerous GP rupture models produces particle-velocity seismograms at each hazard site (Maechling *et al.*, 2007; Callaghan *et al.*, 2008, 2014). CyberShake studies have computed hundreds of thousands of synthetic seismograms at sites spread over central and northern California, specifically, 365 sites in Callaghan *et al.* (2015), 438 sites in Callaghan *et al.* (2017), and 869 sites in Callaghan *et al.* (2018). More recent applications have been focused on the hybridization of CyberShake results by including higher-frequency stochastic ground motions with application primarily in dynamic analysis of structural and geotechnical systems (Callaghan *et al.*, 2020).

This study constitutes one of the first studies toward applying the CyberShake platform outside California (note that Bradley *et al.*, 2018, employed a different computational framework using forward simulations for physics-based PSHA in New Zealand). In the following, we first describe the tectonic setting and seismological characteristics of the Southwest Iceland transform zone. We then present details toward the migration of CyberShake to the regional earthquake source scaling in Southwest Iceland, in particular the calibration of the rupture generator to a local earthquake magnitude–area scaling law and crustal velocity and density models scaling. We apply the physics-based earthquake rupture forecasting model of the SISZ–RPOR transform zone to generate a realization of a finite-fault earthquake rupture forecast equivalent to a 500-yr-long synthetic earthquake catalog, covering earthquake moment magnitudes in the range of M_w 5–7. We then apply the GP earthquake rupture generator in the simulation of multiple rupture variations of each earthquake in the finite-fault catalog, and in the kinematic simulation of the seismic ground motions on a rectangular grid of 625 hypothetical stations in Southwest Iceland. This simulation employs a 5 km interstation spacing. Thus, for each earthquake fault rupture variation and each hypothetical station, two horizontal-component synthetic seismic time histories are simulated, each one using a 0–1 Hz point source polarized along one of the two horizontal grid directions. Key strong motion intensity measures are then derived from the time histories, including peak ground velocity and pseudoacceleration spectral response (PSA) estimates of single-degree-of-freedom oscillators of natural periods from 2 to 10 s. We validate the results by comparing the PSA with magnitude–distance-dependent empirical ground-motion prediction equations (GMPEs) derived from regional strong motion data. Finally, we examine the fundamental characteristics of the synthetic motions in the near-fault region. It is worth mentioning that this work is limited to the generation of a large set of ground-motion seismograms and intensity measures, by modeling events prescribed by a physics-based seismic catalog developed for South Iceland, making such ground-motion synthetics readily available for PSHA studies.

THE SOUTHWEST ICELAND TRANSFORM ZONE

Tectonics of the bookshelf fault system

The transcurrent tectonic plate motion across the Southwest Iceland transform zone is oriented east–west along the RPOR and SISZ. However, instead of a large east–west-aligned sinistral strike-slip fault, the release of tectonic strain is accommodated on short near-vertical dextral strike-slip faults striking north–south, perpendicular to the transcurrent axis (see Fig. 1). This has been conclusively confirmed in past studies that have mapped old surface fault traces, relative relocations of localized seismic swarms, inferred fault locations of large historical earthquakes, along with macroseismic felt area extent and orientation from historical accounts, and detailed source and strong motion studies of recent M_w 6.3–6.5 earthquakes in 2000 and 2008 (e.g., Einarsson, 1991, 2010; Morgan and Kleinrock, 1991; Stefánsson *et al.*, 1993; Clifton *et al.*, 2003; Pagli *et al.*, 2003; Pedersen *et al.*, 2003; Árnadóttir, 2004; Roth, 2004; Dubois *et al.*, 2008; Halldorsson and Sigbjörnsson, 2009; Hjaltadóttir, 2009; Hreinsdóttir *et al.*, 2009; Decriem *et al.*, 2010; Einarsson *et al.*, 2020; Steigerwald *et al.*, 2020).

The average distance between faults in southwest Iceland appears to be ~5 km (Stefánsson *et al.*, 2006), but there is evidence that these interfault distances decrease toward the west in the RPOR, even down to a few hundred meters (Steigerwald *et al.*, 2020). Hypocentral distributions of small earthquakes in the SISZ and the RPOR are mostly at 1–5 km depth in the western part of the RPOR but the seismogenic depth increases gradually toward the east, culminating at a maximum of 12–15 km depth in the easternmost part of the SISZ (Stefánsson *et al.*, 1993; Einarsson, 2014; Panzera *et al.*, 2016; Steigerwald *et al.*, 2020). As a result, the seismogenic potential of the zone increases toward the east, in agreement with the historical earthquake catalog (Einarsson *et al.*, 1981; Dubois *et al.*, 2008; Panzera *et al.*, 2016).

All strong historical earthquakes in Southwest Iceland that have caused damage are considered to have occurred on the bookshelf fault system, with volcanic earthquakes in the RPOR being smaller and thus contributing little to the PSHA in the region. However, reliable earthquake catalogs for subzones of different maximum potential earthquake magnitudes are relatively sparse, in particular along the RPOR. A physics-based model of the bookshelf earthquake fault system in the Southwest Iceland transform zone has been developed (Bayat *et al.*, 2022). It has been calibrated to the rate of tectonic transform motion across the zone and constrained by the geometry of the fault system and the variation of seismogenic potential along the transform zone. The model allows random realizations of the fault system configuration where distance between faults is varied, with the model specifying each fault dimensions, maximum potential seismic magnitude, and long-term slip and moment rate, along with parametric uncertainty estimates. The model allows the derivation of subzone-specific MFDs, the cumulative seismic activity of which is not only

consistent with, but effectively explains, the long-term earthquake catalog of the Southwest Iceland transform zone (Bayat *et al.*, 2024). The model has recently been applied to generate realizations of long-term finite-fault earthquake rupture forecasts (earthquake catalogs) and used for point estimates of PSHA at representative far-field and near-fault sites, albeit using conventional methods based on empirical GMPEs (Kowsari *et al.*, 2023). However, finite-fault earthquake catalogs are much more useful for a physics-based approach to PSHA, through earthquake rupture modeling and seismic ground-motion simulations, using either the dynamic or kinematic modeling approach.

METHODOLOGY AND LOCATION

Earthquake physics-based simulations require realistic inputs to provide reliable outcomes. The fundamental parameters are related to the description of the (an)elastic physical properties of the subsurface and the detailed description of space–time energy sources, typically slip and slip rate on a fault. The specific description of such parameters (e.g., discretization, smoothness) is related to the numerical method used for the simulations and its implementation. Moreover, when assessing the expected ground motion for more than a single specific earthquake, we need to populate a synthetic catalog, characterized by locations, magnitudes, and fault mechanisms. Finally, a series of sites of interest, which may or may not coincide with existing seismic stations is needed to obtain the synthetics records for further analysis. The whole workflow then needs to be orchestrated, typically on an HPC system. The details of the methods and processes involved are presented in the following.

Pseudodynamic fault-rupture model

The kinematic rupture description of an earthquake source prescribes the spatial and temporal evolution of the slip vector across the fault surface. A pseudodynamic kinematic rupture description is expected to abide by well-known principles of seismic faulting dynamics to constrain, for example, source time functions, rise time, or slip rate (e.g., Thingbaijam *et al.*, 2017). The GP (Graves and Pitarka, 2010, 2016) rupture generators fall into this category while being able to produce full kinematic models including, for example, the dependence of rupture velocity and slip rate with depth and abiding to a prescribed magnitude, fault orientation, area, and depth. Regarding the asperity-size scaling law, the GP methods depend on Von Karmann filters applied to initial random slip distributions. For the purposes of the current study, we adopt the asperity size scaling law proposed by Mai and Beroza (2002),

$$\log(a_S) = -2.5 + \frac{1}{2}M_w, \quad \log(a_D) = -1.5 + \frac{1}{3}M_w, \qquad (1)$$

in which a_S and a_D are the correlation lengths (units in km) along the fault-strike and fault-dip directions, respectively. The correlation coefficients $a_S = -2.5$ and $a_D = -1.5$ allow a GP generation of slip models exhibiting asperity sizes roughly consistent with regional slip inversions. This important rupture generation feature is better realized by the Graves and Pitarka (2016) method's version, which is finally employed in this study. By design, CyberShake applies the concept of rupture variations for GP generation of kinematic rupture models, to better account for uncertainties in the hypocenter location. Specifically, for each rupture prescribed in the input ERF, the hypocenter location is uniformly varied along the seismogenic fault plane according to a fixed variation step of 4.5 km, along both the strike and dip directions. The different ruptures resulting from this variation of the hypocenter location are hereafter labeled "rupture variations." The number of rupture variations varies with earthquake magnitude. For events of $M_w \sim 5$–6.1 in this study, there are around nine rupture variations (RVs) on the average for each synthetic finite fault of the earthquake rupture forecast. At $M_w \sim 6.3$ there are ~10 RVs, at $M_w \sim 6.6$ there are ~12–13 RVs, and at M_w 6.8–7 there are ~15 RVs.

Generally speaking, the GP methods estimate kinematic rupture parameters using empirical relations based on observations and derived statistical analyses. The resulting slip maps satisfy a prescribed seismic moment and exhibit heterogeneities along the given fault area arising from Von Karman correlation (see equation 1). The reduction of rupture speed Vr at shallow depths observed in earthquake sliding is considered by setting Vr as a variable fraction of the local shear-wave velocity β (Vr~0.8 β below 8 km depth, whereas Vr ~0.56 β above 5 km, and finally a linear transition establishes a smooth transition of Vr for depths in the interval [5, 8] km). This background Vr estimation is used by a travel-time simulation scheme to build an initial fault distribution of rupture times. A perturbation that is directly dependent on the local slip is added to the initial rupture time of each subfault in favor of source variability. Similarly, a square root scaling relation leads to an initial rise time distribution, which is later perturbed through a spatial random field correlated with fault slip. The GP methods also allow for modeling variability of the slip orientation and fault roughness. In the first case, a variable rake distribution is built by adding a random field that satisfies a Von Karman correlation function to the value provided by the input focal mechanism (FM). Thus, rake variations across the fault roughly present a standard deviation of 15°. Alternatively, a roughness perturbation model for the fault surface is designed in the wavenumber domain, which obeys a self-similar fractal distribution over a bandwidth depending on fault length. The spatially transformed roughness model quantifies the perturbation of each subfault surface, and then determines the variation of the local strike and dip, relative to the reference FM values. These GP models' features seek to mimic real earthquake ruptures making them suitable for realistic ground-motion simulations.

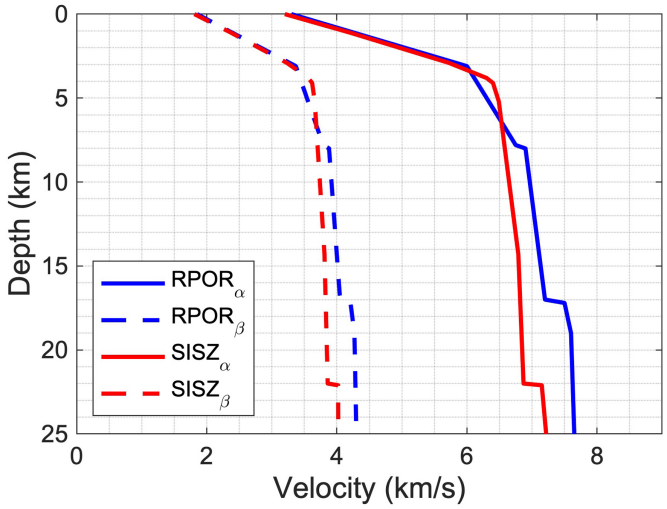

Figure 2. The 1D velocity models for the RPOR and the SISZ regions (Vogfjörd *et al.*, 2002) used in the fault rupture and ground-motion modeling in this study. The color version of this figure is available only in the electronic edition.

3D wave-propagation simulation solver

The wave-propagation solver available in CyberShake is the finite-difference velocity–stress staggered-grid anelastic wave propagation (AWP–ODC) code (Anelastic Wave Propagation with additional suffixes from code authors Olsen, Day, and Cui; Cui *et al.*, 2010, 2013), with fourth-order spatial accuracy coupled to a second-order leapfrog time-marching scheme. This code has been highly optimized to perform site-to-fault reciprocal simulations for computing the SGTs along all fault planes (Jordan and Callaghan, 2018). Alternative code versions perform standard forward fault-to-site earthquake simulations (Cui *et al.*, 2010), which have also been efficiently implemented in parallel architectures. Although the main AWP–ODC limitation of modeling flat topographies has recently been overcome using curvilinear coordinates (O'Reilly *et al.*, 2022), the present study is limited to flat topography as the SISZ–RPOR topography is relatively flat and the frequency range of ground-motion simulations [0,0.5] Hz would have been ineffective in accounting for the minor topography variations. We use standalone fault-to-site configurations for single-event validation studies and CyberShake-integrated site-to-fault configurations for massive multievent cases. No numerical difference is expected between the two configurations. For all cases, we have used nine points per minimum S wavelength that allows highly accurate results up to our prescribed cutoff frequency of 1 Hz.

Implementation framework

The installation of the CyberShake platform at the Marenostrum 4 Supercomputer is the result of a collaboration between the Statewide California Earthquake Center (SCEC) and the Barcelona Supercomputing Center (BSC–CNS, Centro Nacional de Supercomputación) and other partners in the framework of the ChEESE Center of Excellence (Folch *et al.*, 2023). In order to run Cybershake in Marenostrum, the UnifiedCSWflow open-source workflow manager was developed (Rojas *et al.*, 2022). It organizes the end-to-end execution process according to data dependencies of the CyberShake workflow and effectively replaces the original workflow based on Pegasus and HTCondor for the current application. UnifiedCSWflow handles the CyberShake relational database that stores the input ERF data, the identification metadata of each processing step, and the large amount of output SGTs and hazard intensities. UnifiedCSWflow capabilities suffice for performing CyberShake earthquake modeling in the RPOR–SISZ region given its simpler parameterization in terms of one single input velocity model and our moderate size earthquake rupture forecast (as detailed in the next section). However, a complex operational workflow has been implemented by SCEC, to use the whole CyberShake platform for building PSHA models in California through computationally extensive executions across leadership-class supercomputers (Callaghan *et al.*, 2024).

Velocity and density model

A fundamental requirement for earthquake physics-based seismic simulations is an accurate model of the properties of the subsurface. Specifically, we need a representation of the compressional wavespeed α, material density, and attenuation, in addition to the spatial distribution of β. Our study area comprises both the RPOR and SISZ regions. For each region, we used the corresponding 1D P- and S-wave velocity models, as seen in Figure 2 (Vogfjörd *et al.*, 2002). The models show that the upper crust has a minimum shear wavespeed of ~1.9 km/s at the surface and with a steep gradient to depths of 3–4 km, followed by a lower crust with a smooth increase of velocity in the depth range 16–22 km. For the purpose of seismic simulations, the models need to be coupled and smoothed. For the first task, we have included a 10-km-wide crossover zone starting at longitude −21.38° toward the west, in which α and β are linearly harmonic averaged to avoid undesired numerical artifacts. For the resulting velocity model, density is estimated following the empirical law for Icelandic rocks by Darbyshire *et al.* (2000). Along depth, we have applied Gaussian smoothing to the three elastic properties, where P- and S-wave slownesses are smoothed instead of the velocity to preserve travel time. For our South Iceland study, we use viscoelastic attenuation parameters employed in viscoelastic ground-motion simulations in California, with $Q_S = 0.05\beta$ (β in m/s) and $Q_P = 2Q_S$. Seismic wave amplification due to site effects is omitted as localized site amplification in Iceland is generally slight (Rahpeyma *et al.*, 2023; Darzi *et al.*, 2024) as the rock-site classification of relatively high shear wavespeed ($V_{S30} > 750$ m/s) is prevalent in Iceland and soft sedimentary deposits are rare and geographically localized (Sigbjörnsson *et al.*, 2014; Rahpeyma *et al.*, 2023; Darzi *et al.*, 2024).

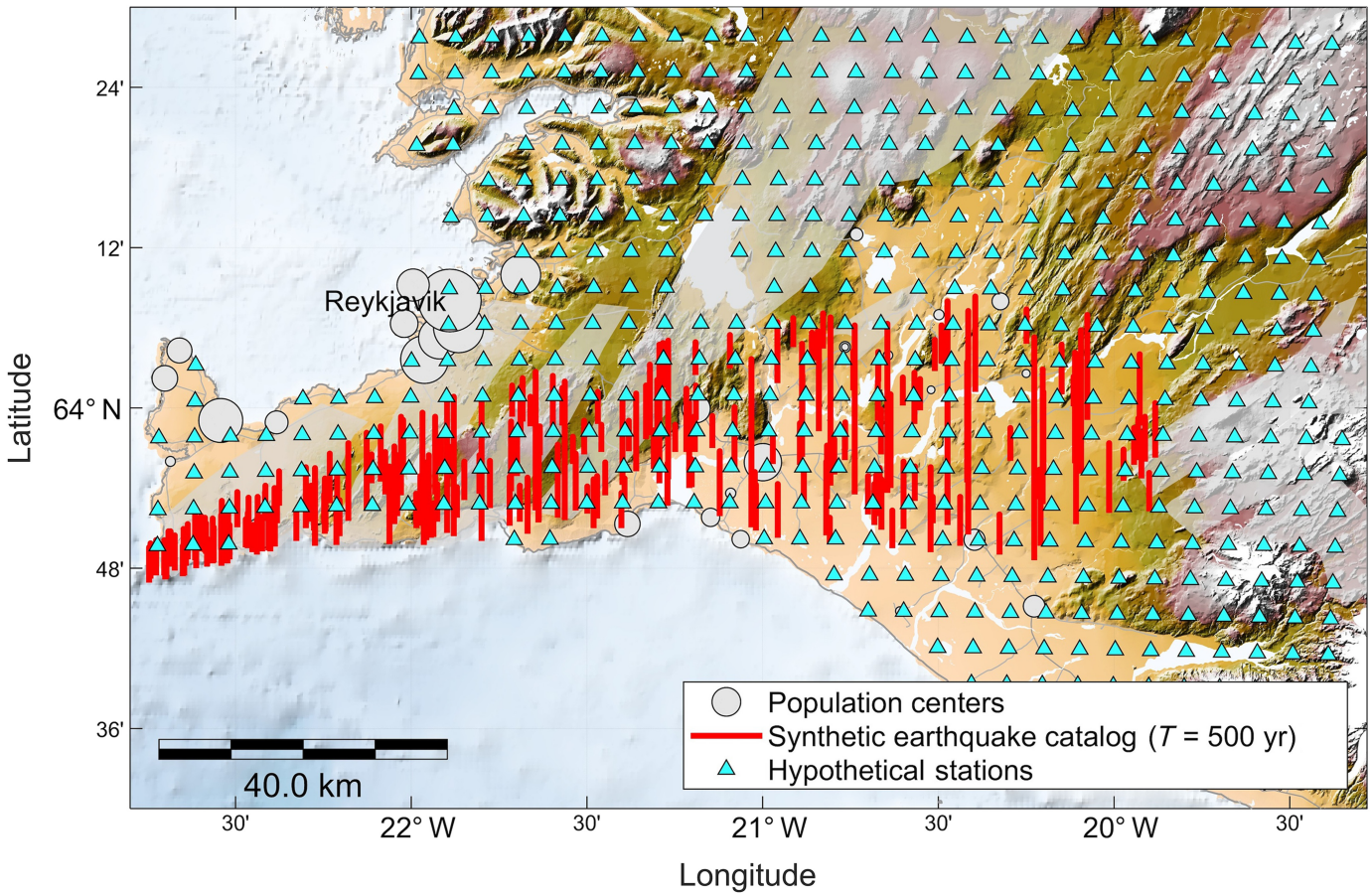

Figure 3. Physics-based simulation domain in Southwest Iceland. The hypothetical station grid consists of 625 sites and the realization of the RPOR–SISZ earthquake rupture forecast (ERF) used in the simulations comprises 223 north–south-striking dextral vertical strike-slip fault planes (red lines). The color version of this figure is available only in the electronic edition.

The earthquake rupture forecast

The recurrence time of the largest earthquakes ($M_w \sim 7$) in the Southwest Iceland transform zones is about 100–150 yr. This is attested to by the historical (e.g., Tryggvason *et al.*, 1958; Stucchi *et al.*, 2013; Einarsson, 2014) and instrumental catalogs (Ambraseys and Sigbjörnsson, 2000; Grünthal *et al.*, 2013; Jónasson *et al.*, 2021). We follow the work of Bayat *et al.* (2022, 2024) and Kowsari *et al.* (2022) that developed a fault system model of the Southwest Iceland transform zone (SISZ–RPOR), that was calibrated to the rate of tectonic transform motion in the region, and generate realizations of a long-term synthetic finite-fault ERF in the form of time-independent earthquake catalogs. For this study therefore, we have generated a 500-yr-long earthquake rupture forecast of sufficient duration to contain a few maximum magnitude earthquake scenarios, resulting in a total of 223 events, the minimum and maximum magnitudes of which are M_w 5 and 7, respectively, the latter being the maximum magnitude generally considered for the eastern SISZ. Namely, for each subzone of the transform zone (see Fig. S1, available in the supplemental material to this article), we generate a 500-year synthetic finite-fault catalog with an MFD that conforms to the subzone MFD derived from the SISZ–RPOR fault system model (Bayat *et al.*, 2022), which is consistent with the MFD derived from the subzone's historical seismicity (Bayat *et al.*, 2024) (see Fig. S2). In other words, the number of ruptures of equivalent magnitudes in each subzone are determined by the respective subzone MFDs and are not uniformly distributed. The locations of the synthetic faults are simulated by a uniform random distribution over the subzone spatial extent to sample the uncertainty and variability of fault locations (Kowsari *et al.*, 2023). The synthetic earthquakes are confined to single fault ruptures in this study, although recent observations show that multifault rupture on parallel adjacent bookshelf faults can take place in the zone (e.g., the M_w 6.3 earthquake of 2008, Decriem *et al.*, 2010). The total MFD of the earthquake rupture forecast conforms to that derived from the most comprehensive long-term seismic catalog observed for the Southwest Iceland transform zone (shown in Fig. S2). Our validation of CyberShake ground-motion simulations thus considers the magnitude range of expected moderate-to-large events in the region and captures the spatial variation of seismogenic potential along the zone, that is, increasing maximum earthquake magnitude from $M_w \sim 5.5$ in the western part of the RPOR to $M_w \sim 7$ in the eastern part of the SISZ (see Fig. S1).

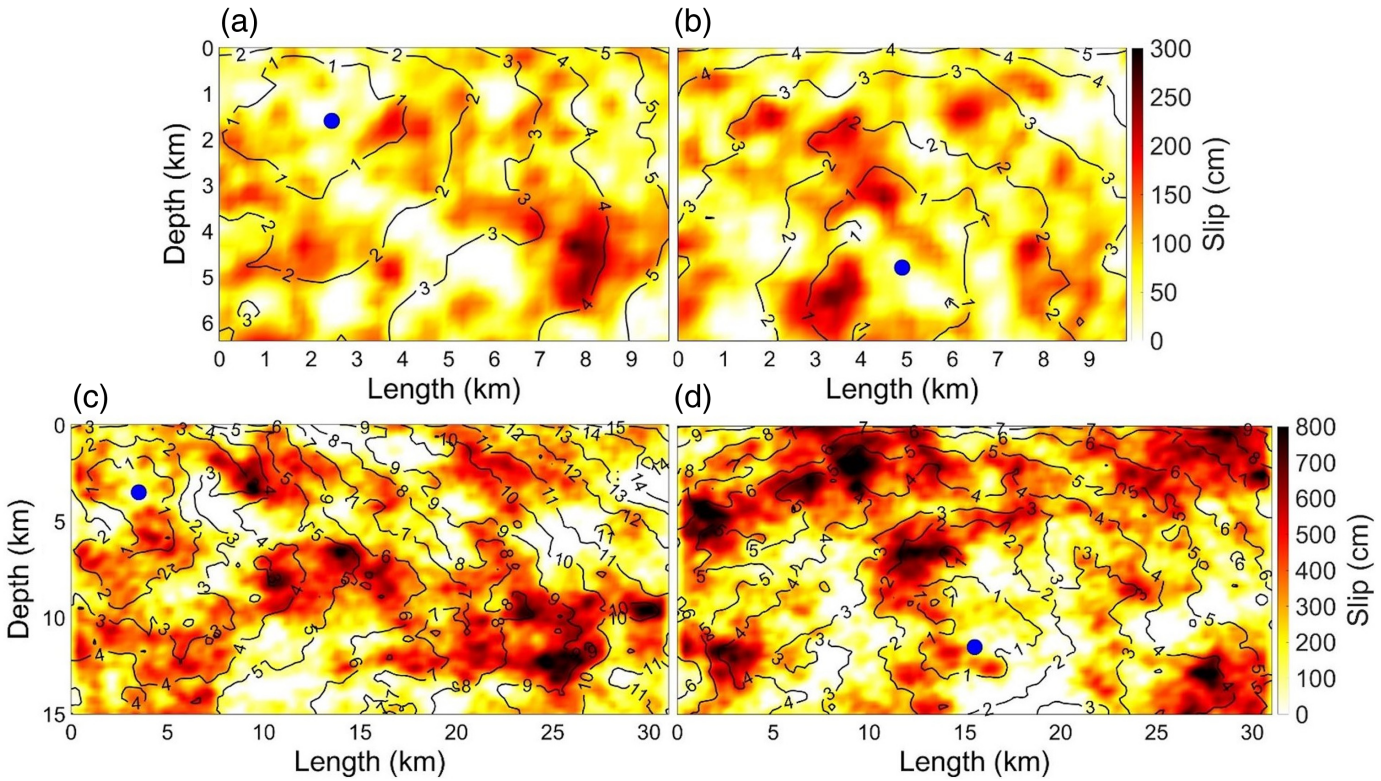

Figure 4. Two examples of rupture variations of (a,b) M_w 6 and (c,d) 7 earthquakes from the synthetic finite-fault earthquake catalog. Each rupture variation is defined by different realizations of random slip distributions and different hypocentral location on the fault plane. The examples shown correspond to a (a,c) unilateral (toward north) rupture with a shallow hypocenter and (b,d) bilateral fault rupture with a deep hypocenter. The color version of this figure is available only in the electronic edition.

Uncertainty in fault locations along the RPOR–SISZ zone is sampled in the synthetic earthquake catalog for the physics-based simulations by selecting random locations within each zone around the centerline of the tectonic plate margin constrained by the locations of the historic and instrumental seismicity and extent of mapped and inferred faults in the region. Figure 3 shows the rupture extents of the finite-fault earthquake catalog used in this work that comprises 223 parallel north–south, near-vertical dextral strike-slip faults. Thus, this synthetic finite-fault earthquake catalog facilitates physics-based simulations of the low-frequency seismic motions.

Notably, the earthquake magnitude–area scaling in the Southwest Iceland transform zone does not follow most common scaling laws of shallow crustal interplate strike-slip earthquakes (e.g., those in Wells and Coppersmith, 1994; Mai and Beroza, 2000). The estimated fault extent of historical earthquakes, and in particular those of the recent M_w 6.3–6.5 earthquakes in 2000 and 2008, show a much smaller relative fault area and relatively larger slip than expected by most scaling laws (see, e.g., Pedersen *et al.*, 2003; Dubois *et al.*, 2008; Hreinsdóttir *et al.*, 2009; Decriem *et al.*, 2010) (see Table S1). However, the "effective source area" scaling law of shallow crustal interplate strike-slip earthquakes of Mai and Beroza (2000) has been found to describe well the total area of earthquakes in the SISZ–RPOR and has been applied here in accordance with the original study (Bayat *et al.*, 2022) and subsequent applications (Kowsari *et al.*, 2023; and in particular Li *et al.*, 2023) (see Fig. S3 and Table S1).

We show in Figure 4 examples of two rupture variations for a hypothetical M_w 6 (Fig. 4a,b) and 7 (Fig. 4c,d) events, occurring on different faults. The synthetic catalog provides the associated fault and magnitude for each of these events. These plots illustrate the corresponding slip maps for two rupture variations, that is, hypocentral location and slip, in the CyberShake terminology. These variations exemplify the salient characteristics of the earthquake source scaling as implemented in the GP kinematic rupture generator used in this study for the SISZ–RPOR. This is done in accordance with slip inversion studies of recent strong earthquakes in Southwest Iceland, which are characterized by relatively small total rupture area and large slip for the given magnitudes. However, our preferred moment–area relationship for southern Iceland likely results in larger ground motions, specifically in the near-fault region, than those obtained from this version of the GP rupture generator and is assessed using comparisons against GMPEs. Further work is, however, needed, which is beyond the scope of this study, to confirm the suitability of the overall source scaling, in particular for near-fault motions.

RESULTS

We run physics-based simulations up to 0.5 Hz using an updated 1D velocity model of the RPOR–SISZ region, as described above. A total of 2103 rupture variations are

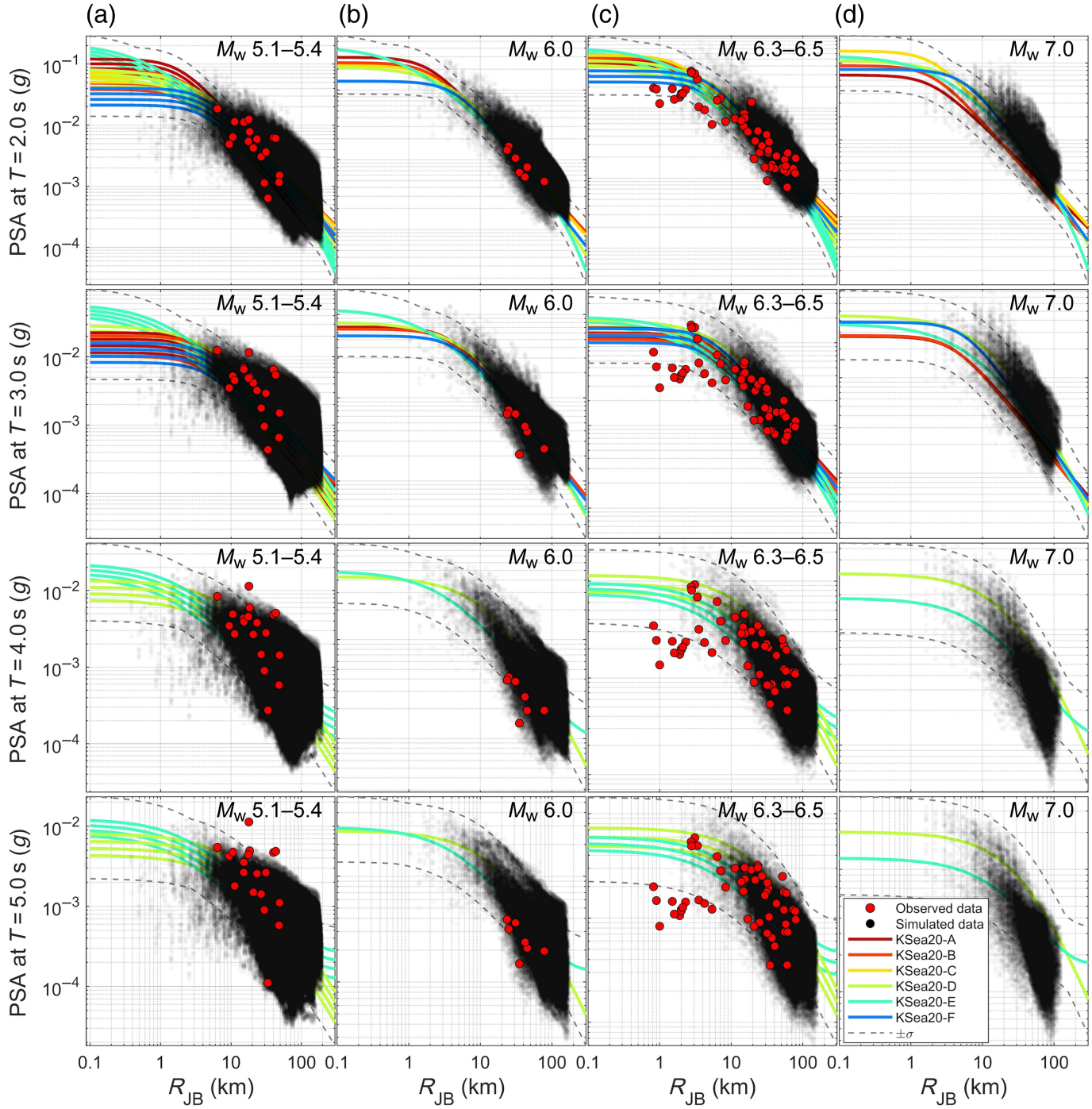

modeled each with two horizontal components of seismic ground-motion time histories per site. We compare the simulated ground-motion intensity measures to a set of empirical GMPEs recently developed for this region (Kowsari *et al.*, 2020). As the ground-motion parameter predicted by the GMPEs is the rotational invariant measure (RIavg; Rupakhety and Sigbjörnsson, 2013) of the PSA from the two horizontal time-history components, we calculate the same measure from the synthetic ground motions at each station. The comparison of the synthetic strong motion data set to the GMPEs is shown in Figure 5. The results have been plotted in terms of the two

Figure 5. CyberShake ground-motion scaling with magnitude and fault distance for the Southwest Iceland transform zone. (a–d) The synthetic pseudoacceleration spectral response (PSA, black circles) values at four discrete periods of oscillation (T = 2, 3, 4, and 5 s, top to bottom rows) and at four magnitude ranges (M_w 5.1–5.4, 6, 6.3–6.5, and 7, left to right columns) are compared with the actual values from the strong motion data set for Southwest Iceland (red circles) and the six empirical ground-motion prediction equations (GMPEs) (KSea20, Kowsari *et al.*, 2020). The ground-motion parameter is the rotation invariant measure of two horizontal PSA estimates. Multiple same color GMPE attenuation curves cover the denoted magnitude ranges in steps of 0.1 magnitude units. The color version of this figure is available only in the electronic edition.

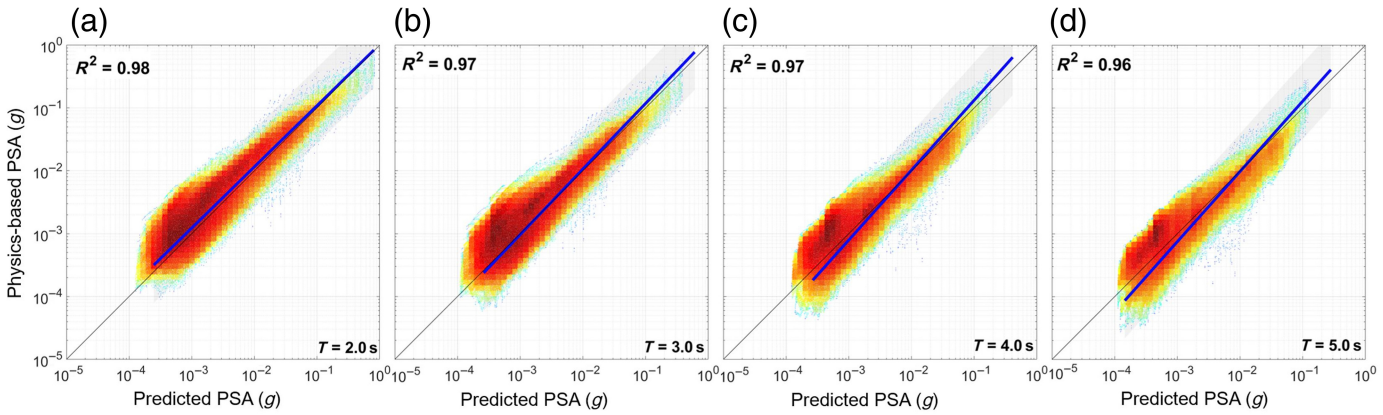

Figure 6. Comparison of the predictions of PSA at four discrete periods (a–d) (2–5 s) by the physics-based simulations (*y*-axis) plotted against the corresponding predictions by the empirical GMPEs (Kowsari *et al.*, 2020). The PSA ground-motion parameter is rotation invariant (RIavg, see the Results section). The points on the scatter plot are colored based on the data density with red regions indicating areas with higher density, and lighter and blue regions indicating sparser data. The blue line is the least-square straight line fit to the points and the correlation coefficient is shown for each period. The gray area denotes the region where predictions are within a factor of 3 of the observations. The color version of this figure is available only in the electronic edition.

independent key parameters of the empirical GMPEs, moment magnitude M_w and R_{JB}, the shortest horizontal distance from a site to the vertical surface projection of the fault. The comparison is made in terms of PSA at oscillator periods of 2–5 s, and at four magnitude bins/ranges, M_w 5.1–5.4, 6, 6.3–6.5, and 7. These magnitudes reflect mainshock seismic ground-motion recordings in the Icelandic strong motion data set for Southwest Iceland (red dots in Fig. 5). In contrast, the intensity measures from the physics-based simulations, that is, the discrete values of PSA at each station are shown as black dots. The comparison highlights the small number of actual earthquake strong motion recordings in the Southwest Iceland transform zone, and the fact that no data exist in Iceland for earthquakes larger than M_w 6.5. The empirical GMPEs have been developed based on the local data set, but these limitations have been alleviated somewhat through Bayesian inference using informed priors of magnitude–distance scaling from other GMPEs calibrated to strong motion data from shallow crustal earthquakes in other interplate regions. The GMPEs are unbiased against the data set (for details, see Kowsari *et al.*, 2020) and their mean predictions are shown for comparison along with their $\pm 1\sigma$ envelope around the mean. We note that multiple GMPE attenuation curves shown in Figure 5 cover the denoted magnitude ranges in steps of 0.1 magnitude units.

The recorded data and the physics-based data set overall show a very good agreement in the magnitude range M_w 5.0–6.5. The same is the case for the comparison against the mean GMPE predictions, which have been shown to be unbiased against the Icelandic strong motion data set (Kowsari *et al.*, 2020). The vast majority of the physics-based results fall into a ± 1 standard deviation band around the GMPE mean value predictions, which effectively validates its migration to the SISZ–RPOR region. We note the comparison at M_w 7 where the GMPEs appear to underpredict the PSA synthetic data at periods of 2 and 3 s over the entire distance range. However, at longer periods, the agreement is better overall, although the attenuation of the long-period response spectral values appears to be larger with distance than that of the GMPEs. Because the GMPEs are not constrained by local data at these large magnitudes, or large distances (>100 km), the physics-based results may play an important role in constraining them for future applications. We note that not all the GMPEs were calibrated to such long periods and, as a result, fewer GMPEs are compared with the data at those periods.

Quantifying further the consistency of the physics-based simulations with the GMPEs, we show in Figure 6 the rotation invariant PSA at T = 2, 3, 4, and 5 s, for the physics-based simulations (*y*-axis) versus the mean prediction from the Kea20 GMPEs (*x*-axis) (Kowsari *et al.*, 2020). On average, the agreement between the physics-based simulations and Kea20 is quite good and supports the validity of the CyberShake approach in the SISZ–RPOR. The results imply a relatively wide variability of the physics-based simulations. Most points, however, seem to cluster around the diagonal with the plots for 2 and 3 s period suggesting that Kea20 may slightly underpredict the synthetic PSA on the average. The clustering of points around this line for periods of 4 and 5 s suggests a better alignment of predicted values with the synthetic data set. Moreover, analyses of the interevent and intraevent residuals of the physics-based data set versus that predicted by the GMPEs are provided as Figures S4–S11. In essence, the residual distributions show the same salient features as shown in Figure 6. In particular, in the magnitude and distance ranges where most of the Icelandic strong motion data are located ($R_{JB} \sim$ 15–55 km and M_w 6.3–6.5), the physics-based simulations are effectively unbiased against the average predictions of the ground-motion models. At larger magnitudes, the GMPEs appear to slightly underpredict the physics-based

simulations, and slightly overpredict at smaller magnitudes. We note that this warrants further investigation in future works, as no data exist in the SISZ for $M_w > 6.5$. Rather few events also exist at M_w 5–5.5, and therefore the physics-based approach holds promise to inform the next generation of Bayesian empirical GMPEs (based on Kowsari *et al.*, 2019, 2020; Rahpeyma *et al.*, 2023), in particular for efforts of increasing the maximum frequency of simulations of this study (0.5 Hz).

We note that from 2 to 5 s period the GMPEs appear to increasingly overpredict the observed PSA amplitudes in the extreme near-fault region of the M_w 6.3–6.5 earthquakes ($R_{JB} \sim 1$–3 km). The observations are all from three strong earthquakes in the SISZ, the 17 June 2000 M_w 6.4, 21 June 2000 M_w 6.5, and 29 May 2008 M_w 6.3 earthquakes, the near-fault velocity pulses of which all show similar features (Halldórsson *et al.*, 2007, 2011; Halldórsson and Sigbjörnsson, 2009). Specifically, the energy of the near-fault data is driven by the near-fault velocity pulses that have a fundamental pulse period of $T \sim 1.5$–2 s and moreover have a narrowband pulse character, that is, rather devoid of energy at longer periods (Halldórsson *et al.*, 2007). The pulse period is controlled primarily by the characteristic dimension of the main slip patch on the fault plane generating the velocity pulse (Mavroeidis and Papageorgiou, 2003; Mavroeidis *et al.*, 2004). The narrowband nature of the Icelandic near-fault pulses thus implies a dominant characteristic dimension of the slip patch on the causative fault plane, and relatively smooth slip. Indeed, this is the case from multiple studies that inferred the static slip distributions from ground motion and deformation data (see Pedersen *et al.*, 2003; Dubois *et al.*, 2008; Hreinsdóttir *et al.*, 2009; Decriem *et al.*, 2010). We therefore expect that M_w 6.3–6.5 earthquakes, that have subevents of relatively small dimensions compared to what is expected for larger earthquakes (e.g., M_w 7), primarily have seismic wave energy around their pulse periods and not at longer periods. The synthetic (physics-based) PSA amplitudes for M_w 6–7 earthquakes, however, do not appear to show such characteristics, which by analogy implies that their energy content is broader, and that the near-fault data are generated by slip patches of greater variability in their dimensions (which is in fact observed in the examples in Fig. 4). This is a positive feature of the GP slip distributions, and we note that the built-in randomization features of the source specification (e.g., subfault strike, dip, and rake are allowed to vary within a range) may have weakening effects on ground-motion coherence at near-fault locations. Finally, we note that the predominant east–west spatial distribution of the Icelandic strong motion network means that the observations are almost exclusively along the fault normal of the causative faults in the SISZ (see Fig. 7). In other words, there were no stations that captured the directivity pulses that were radiated away from the fault ends (along strike toward north and south) of the bilateral fault rupture, that appears to be the primary rupture process of SISZ strong earthquakes (Sigbjörnsson *et al.*, 2014).

In Figure 7, we show the near-fault velocity ground-motion time histories of the 21 June 2000 M_w 6.5 earthquake in the South Iceland seismic zone. The traces show the fault-normal component of velocity derived from the baseline-corrected acceleration time histories recorded at the three stations (red triangles) in the near-fault region of the causative fault (red line) on which a bilateral rupture took place (yellow star denotes the epicenter). For the sake of comparison, we show an example of three M_w 6.5 bilateral rupture variations on a hypothetical finite fault of the ERF (blue fault), complete with static slip distributions and rupture contours. Finally, we compare the corresponding fault-normal synthetic velocity ground motions on stations near the southern fault end having similar source-site geometries. The salient features of these near-fault velocity ground motions are seen to be captured in this case by the physics-based simulations, but further work is needed to confirm the overall magnitude scaling of near-fault velocity pulse amplitudes and their fundamental periods.

Near-fault recordings in the Icelandic strong motion data set are scarce as Figure 7 indicates, but the physics-based simulations promise to allow a more comprehensive spatial coverage around the synthetic faults of the ERF. As an example, we plot the rotation invariant ground-motion measure of PSA at 2, 3, and 5 s oscillator periods in Figure 8 for an M_w 7 bilateral rupture scenario (analogous to those shown in Fig. 4) where dots indicate the hypothetical station locations. The synthetics show that the greatest amount of energy is at $T = 2$ s period, progressively decreasing with increasing period. The amplitude distribution around the fault shows a concentration of large amplitudes in the extreme near-fault region of the southern end of the bilateral rupture, for this rupture variation. This is consistent with rupture directivity and the fact that most of the fault slip on that particular realization is located in the shallow and southern part of the fault, with the rupture propagating primarily upward. The large amplitudes at the stations next to the southern part of the fault are to different degrees dominated by three slip patches that appear at shallow depth. Scrutiny of the synthetic time histories reveals that the fault rupture generates large-amplitude and long-period near-fault velocity pulses of periods from 2–4 s in this region. Overall, the synthetic near-fault wavefield exhibits greater complexity than has been observed in admittedly the very limited near-fault data recorded in Iceland. That is to be expected as the near-fault motions of the CyberShake data set reflect its sampling of source variability, which is promising for the future analyses and applications of this data set given the large number of finite-fault rupture and synthetic seismic ground-motion simulations.

DISCUSSION AND CONCLUSIONS

We have taken the first steps toward a migration of CyberShake to Southwest Iceland, comprising two main porting steps. From a seismological standpoint, an earthquake

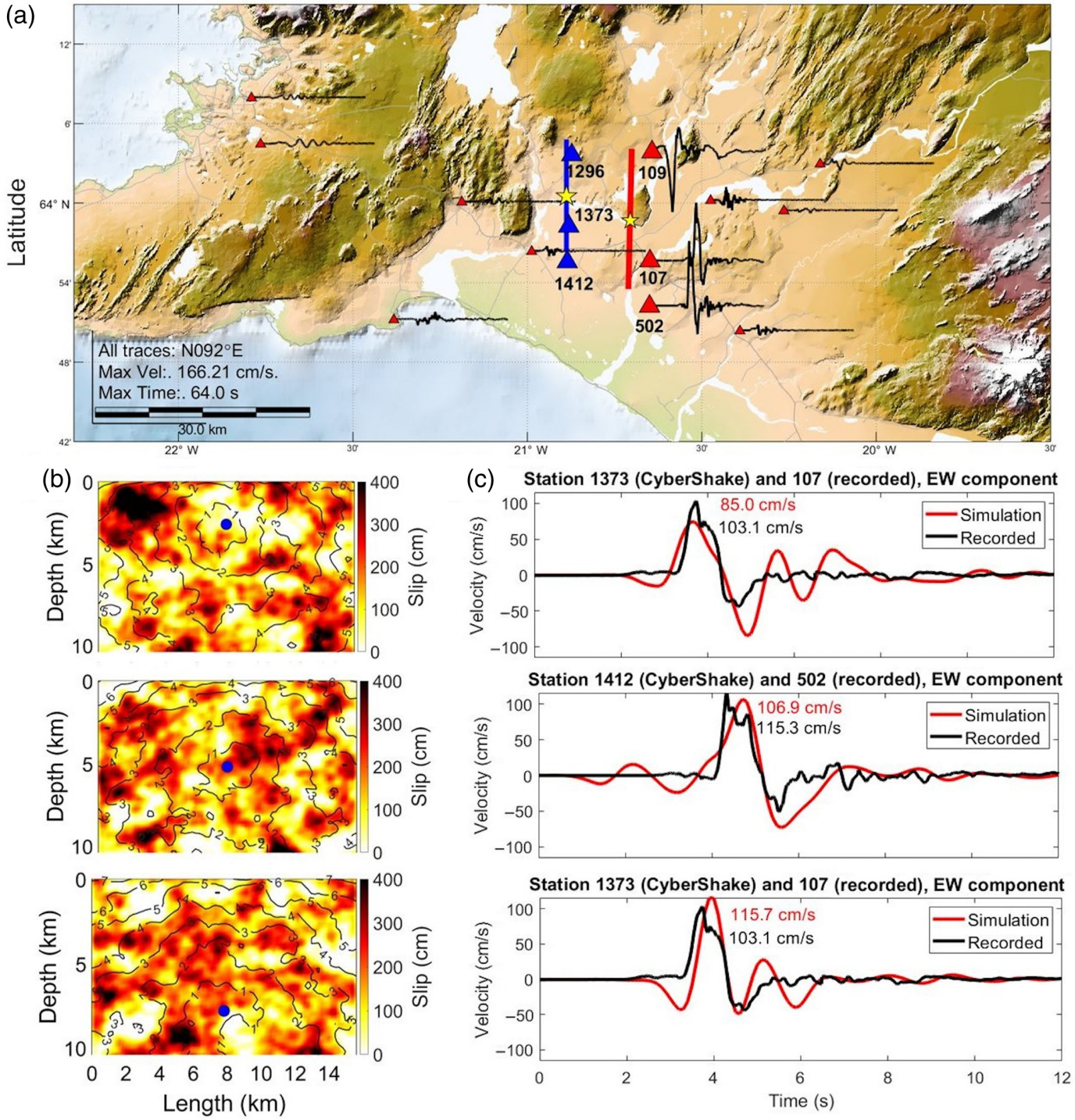

Figure 7. An example of recorded near-fault velocity pulses versus synthetic pulses from our physics-based simulations. (a) Map of southwest Iceland showing the Icelandic Strong Motion Network (ISMN) stations (red triangles), three of which recorded the near-fault motions of the 21 June 2000 M_w 6.5 earthquake. The red line denotes the fault plane of the near-vertical dextral strike-slip fault and the yellow star the epicenter. The black traces show the velocity time histories derived from the baseline-corrected recorded acceleration along the fault-normal direction (west-to-east). For comparison, a synthetic earthquake fault of the same magnitude is shown by the blue line, and (b) three examples of bilateral rupture variations (slip distribution with rupture time contours in seconds, with a blue dot denoting the hypocenter). (c) The corresponding synthetic velocity time histories (red) are compared with the observed velocity time histories at two stations, south of the epicenter. Specifically, the top/middle/bottom rupture variations in panel (b) generated the top/middle/bottom synthetic velocity time histories in panel (c). The color version of this figure is available only in the electronic edition.

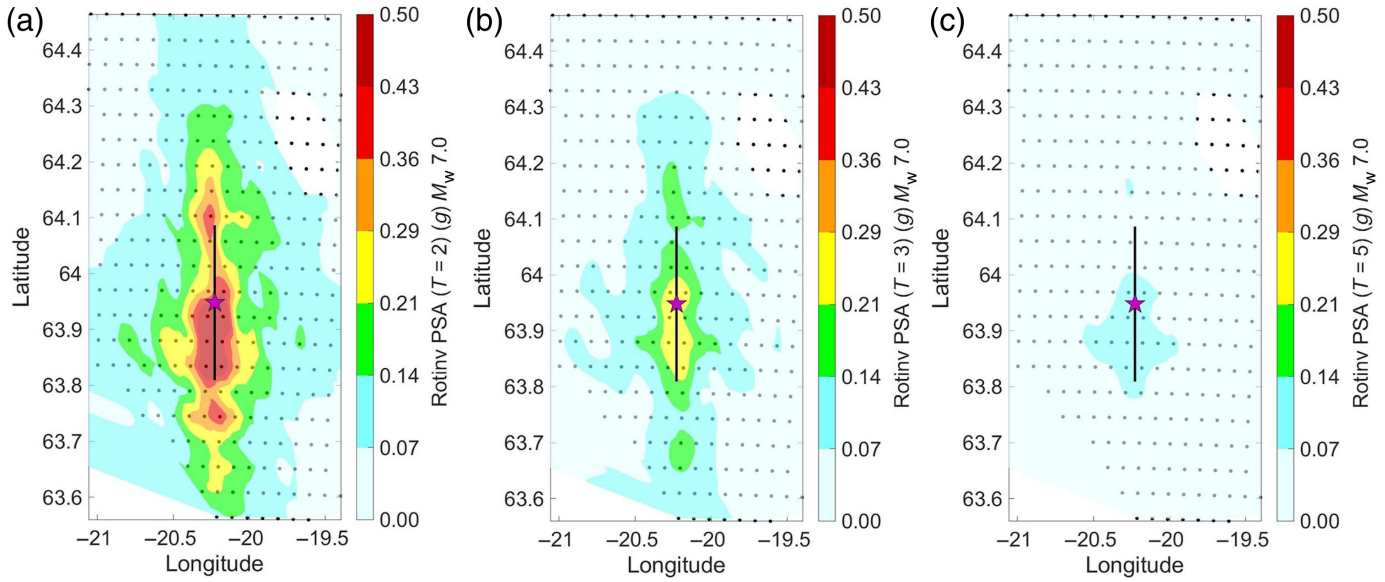

Figure 8. The rotation invariant ground-motion measure of PSA at (a) 2, (b) 3, and (c) 5 s oscillator periods for an M_w 7 bilateral rupture variation similar to those shown in Figure 4. The color version of this figure is available only in the electronic edition.

rupture forecast has been assembled using a synthetic finite-fault and time-independent earthquake catalog corresponding to strong earthquake ruptures on the unique bookshelf fault system of the Southwest Iceland transform zone. The transform zone consists of the SISZ and RPOR zones, and the catalog equivalent to 500 yr of seismicity contains 223 faults of magnitudes between M_w 5 and 7. The spatial variation of the seismogenic potential along the zone is controlled for, in the model, by the six distinct subzones of the SISZ–RPOR bookshelf fault system, each of which has a specific distribution and a maximum earthquake magnitude. The distinct earthquake magnitude–area scaling law for the region has been embedded into the finite-fault catalog. Moreover, slip inversions in SISZ–RPOR have revealed that faulting is mainly characterized by a few large asperities that drive strong near-fault ground shaking. These features of the applied slip distributions are controlled by the Von Karman filter parameters, where we use the recommended values by Mai and Beroza (2002). We show that the method developed by Graves and Pitarka (2016) is suitable for constructing kinematic ruptures for each of the faults of the synthetic finite-fault earthquake catalog. Source variability is explored by varying hypocenter locations along the strike and dip directions in 4.5 km squared cells. Physics-based simulations up to 0.5 Hz (2 s period) have been carried out using a velocity model that results from smoothly coupling the *P*- and *S*-wave profiles from two 1D layered models for the SISZ and RPOR, respectively. A total of 2103 rupture variations (earthquakes) are modeled, and the corresponding two horizontal component time histories of synthetic seismic ground motion simulated at 625 hypothetical sites in Southwest Iceland.

From a technological standpoint, the execution of the physics-based simulations has been highly facilitated by the development of the open source UnifiedCSWflow workflow manager. UnifiedCSWflow handles the whole execution process according to data dependencies of processing steps and controls database access by storing the input earthquake rupture forecast data, the identification of metadata in each processing step and the large number of computed seismograms and ground-motion parameters. In this sense, UnifiedCSWflow has properly replaced the complex original workflow used in California to run CyberShake on BSC's MareNostrum 5 supercomputer.

We compare peak synthetic ground-motion parameters of the physics-based data set in the form of rotation invariant measures of PSA at 2, 3, 4, and 5 s periods to a suite of empirical GMPE models developed for the region (Kowsari *et al.*, 2020). The synthetic magnitude–distance characteristics cover M_w 5–7 and Joyner–Boore distances of less than 1 km to a maximum of ~160 km. The physics-based data set is in very good agreement with the GMPEs, with the vast majority of physics-based results falling within a ±1 standard deviation band around the GMPE mean predictions at most magnitudes. At the largest considered earthquake magnitudes, M_w 7, the GMPEs appear to be slightly underpredicting the PSA values at 2–3 s oscillator periods, whereas the comparison at longer periods shows a better fit. However, as the GMPEs are not constrained by local data at these large magnitudes, the physics-based synthetic data set may play an important role in constraining the GMPEs in future applications. The near-fault amplitudes of selected scenarios show relatively good consistency with rupture variation characteristics, that is, the geometry of the station grid, the hypocenter location on the fault, and the location of the significant slip patches on the fault plane. The characteristics of the synthetic near-fault wavefield indicate much greater complexity than has been observed in

the very limited near-fault data recorded in Iceland to date. Although the favorable comparison of the physics-based ground motions to GMPEs to some extent validates the source scaling used in this study, future studies are required to confirm its overall applicability, in particular for near-fault motions.

We conclude that the consistency of the physics-based synthetic data set of long-period motions with the GMPEs effectively validates its migration to the SISZ–RPOR region. This is a prerequisite for future work, toward increasing the duration of the earthquake rupture forecast and the maximum frequency of the ground motions, so that a statistically consistent and physics-based PSHA study may be carried out in the SISZ–RPOR region, promoting the routine application of Cybershake outside of California.

DATA AND RESOURCES

The supplemental material includes further information on the magnitude–frequency distribution (MFD) of the earthquake rupture forecast and the spatial variation of seismic potential along the Southwest Iceland transform zone. It also provides information on the suitability of the Mai and Beroza (2002) area–magnitude scaling law for the bookshelf faults in the transform zone. Finally, the supplement shows the interevent and intraevent residual distributions at several discrete oscillator periods.

DECLARATION OF COMPETING INTERESTS

The authors acknowledge that there are no conflicts of interest recorded.

ACKNOWLEDGMENTS

The research leading to these results has received funding primarily from the European Union's Horizon 2020 research and innovation programme under the ChEESE project (Grant Agreement Number 823844), the Horizon Europe projects ChEESE-2P (Grant Agreement Number 101093038), DT-GEO (Grant Agreement Number 101058129), and Geo-Inquire (Grant Agreement Number 101058518). B. H. acknowledges partial funding received from the Icelandic Centre for Research (Rannis) Icelandic Research Fund Project Grant (Number 196089, SENSHAZ) and a Doctoral Grant (Number 239376), the Landsvirkjun Energy Research Fund (Number NÝR-04-2023), the Icelandic Road and Coastal Administration Research Fund (Number 1800-947), the University of Iceland Research Fund (Number 92334), and the Horizon 2021 EuroHPC JU-RIA Grant (Number 101093038, ChEESE-2P). A.-A. Gabriel acknowledges additional funding from the European Union's Horizon 2020 Research and Innovation Programme (TEAR ERC Starting, Grant 852992), the National Science Foundation (NSF Grant Numbers EAR-2225286, EAR-2121568, OAC-2139536, OAC-2311208), and the National Aeronautics and Space Administration (80NSSC20K0495). The authors would like to thank Robert Graves, an anonymous reviewer, and the Associate Editor for insightful reviews that improved the article.

REFERENCES

Ambraseys, N. N., and R. Sigbjörnsson (2000). Re-appraisal of the seismicity of Iceland, *Acta Polytech. Scand.* **2000–003,** no. 3, 1–184.

Árnadóttir, T. (2004). Coseismic stress changes and crustal deformation on the Reykjanes Peninsula due to triggered earthquakes on 17 June 2000, *J. Geophys. Res.* **109,** no. B9, doi: 10.1029/2004JB003130.

Árnadóttir, T., W. Jiang, K. L. Feigl, H. Geirsson, and E. Sturkell (2006). Kinematic models of plate boundary deformation in southwest Iceland derived from GPS observations, *J. Geophys. Res.* **111,** no. B7, doi: 10.1029/2005JB003907.

Atkinson, G. M. (2012). Integrating advances in ground-motion and seismic hazard analysis, *Proc. of the 15th World Conf. on Earthquake Engineering, Keynote/Invited Lecture*, Lisbon, Portugal, 24–28 September 2012.

Bayat, F., M. Kowsari, and B. Halldorsson (2022). A new 3-D finite-fault model of the Southwest Iceland bookshelf transform zone, *Geophys. J. Int.* **231,** no. 3, 1618–1633, doi: 10.1093/gji/ggac272.

Bayat, F., M. Kowsari, and B. Halldorsson (2024). A simplified seismicity model of the bookshelf fault system of the Southwest Iceland transform zone, *Bull. Earthq. Eng.* **22,** 4959–4981, doi: 10.1007/s10518-024-01946-5.

Bayraktar, B., C. Özer Sözdinler, Ö. Necmioğlu, and N. Meral Özel (2017). Preparation of Synthetic Earthquake Catalogue and Tsunami Hazard Curves in Marmara Sea using Monte Carlo Simulations, *EGU General Assembly Conference Abstracts*, Vienna, Austria, 23–28 April 2017, 1374 pp.

Bradley, B. A., H. Razafindrakoto, B. Maurer, J. Motha, K. Tarbali, and R. Lee (2018). Simulation-based ground motion prediction of historical and future New Zealand earthquakes and consequent geohazard impacts, *Geotechnical Earthquake Engineering and Soil Dynamics V*, American Society of Civil Engineers, Reston, Virginia, 29–42.

Callaghan, S., C. Goulet, F. Silva, P. Maechling, R. Graves, O. O'Reilly, K. Olsen, A. Kottke, T.-Y. Yeh, and Y. Ben-Zion (2021). Verification and validation of the broadband CyberShake platform, *Eos Trans. AGU* (Fall Meet.), Abstracts S11A-05.

Callaghan, S., P. Maechling, E. Deelman, K. Vahi, G. Mehta, G. Juve, K. Milner, R. Graves, E. Field, and D. Okaya (2008). Reducing time-to-solution using distributed high-throughput mega-workflows-experiences from SCEC CyberShake, *2008 IEEE Fourth International Conf. on eScience*, IEEE, 151–158.

Callaghan, S., P. J. Maechling, C. A. Goulet, K. R. Milner, R. W. Graves, K. B. Olsen, F. Silva, and Y. Ben-Zion (2020). Enhancing CyberShake simulations for engineering applications, *Eos Trans. AGU* (Fall Meet.), Abstracts S068-05.

Callaghan, S., P. J. Maechling, G. Juve, K. Vahi, E. Deelman, and T. H. Jordan (2014). Optimizing CyberShake seismic hazard workflows for large HPC resources, *Eos Trans. AGU* (Fall Meet.), Abstracts IN21C-3720.

Callaghan, S., P. J. Maechling, C. Goulet, K. R. Milner, R. W. Graves, K. B. Olsen, and H. P. Jordan (2017). Cybershake: Bringing physics-based PSHA to central California, *Poster Presentation at 2017 SCEC Annual Meeting*.

Callaghan, S., P. J. Maechling, C. A. Goulet, K. R. Milner, M. Su, R. W. Graves, K. B. Olsen, B. T. Aagaard, K. E. Wooddell, and A. R. Kottke, *et al.* (2018). A SCEC CyberShake Physics-Based Probabilistic Seismic Hazard Model for Northern California, *Poster Presentation at 2018 SCEC Annual Meeting*.

Callaghan, S., P. J. Maechling, G. Juve, K. Vahi, E. Deelman, and T. H. Jordan (2015). Using CyberShake workflows to manage big seismic

hazard data on large-scale open-science HPC resources, *Eos Trans. AGU* (Fall Meet.), Abstracts IN43B-1738.

Callaghan, S., P. J. Maechling, F. Silva, M.-H. Su, K. R. Milner, R. W. Graves, K. B. Olsen, Y. Cui, K. Vahi, and A. Kottke (2024). Using open-science workflow tools to produce SCEC CyberShake physics-based probabilistic seismic hazard models, *Front. High Perform. Comput.* **2,** 1360720, doi: 10.3389/fhpcp.2024.1360720.

Clifton, A. E., C. Pagli, J. F. Jónsdóttir, K. Eythorsdóttir, and K. Vogfjörð (2003). Surface effects of triggered fault slip on Reykjanes Peninsula, SW Iceland, *Tectonophysics* **369,** nos. 3/4, 145–154.

Cui, Y., K. B. Olsen, T. H. Jordan, K. Lee, J. Zhou, P. Small, D. Roten, G. Ely, D. K. Panda, A. Chourasia, *et al.* (2010). Scalable earthquake simulation on Petascale supercomputers, *SC'10: Proc. of the 2010 ACM/IEEE International Conf. for High Performance Computing, Networking, Storage and Analysis*, New Orleans, Louisiana, 13–19 November 2010, 1–20.

Cui, Y., E. Poyraz, K. B. Olsen, J. Zhou, K. Withers, S. Callaghan, *et al.* (2013). Physics-based seismic hazard analysis on petascale heterogeneous supercomputers, *Proceedings of the International Conference on High Performance Computing, Networking, Storage and Analysis*, Denver, Colorado, 17–22 November 2013.

Darbyshire, F. A., R. S. White, and K. F. Priestley (2000). Structure of the crust and uppermost mantle of Iceland from a combined seismic and gravity study, *Earth Planet. Sci. Lett.* **181,** no. 3, 409–428.

Darzi, A., B. Halldorsson, F. Cotton, and S. Rahpeyma (2024). Nationwide frequency-dependent seismic site amplification models for Iceland, *Soil Dynam. Earthq. Eng.* **183,** 108798, doi: 10.1016/j.soildyn.2024.108798.

Decriem, J., T. Árnadóttir, A. Hooper, H. Geirsson, F. Sigmundsson, M. Keiding, B. G. Ófeigsson, S. Hreinsdóttir, P. Einarsson, and P. LaFemina (2010). The 2008 May 29 earthquake doublet in SW Iceland, *Geophys. J. Int.* **181,** no. 2, 1128–1146.

Dubois, L., K. L. Feigl, D. Komatitsch, T. Árnadóttir, and F. Sigmundsson (2008). Three-dimensional mechanical models for the June 2000 earthquake sequence in the south Iceland seismic zone, *Tectonophysics* **457,** nos. 1/2, 12–29, doi: 10.1016/j.tecto.2008.05.020.

Einarsson, P. (1991). Earthquakes and present-day tectonism in Iceland, *Tectonophysics* **189,** nos. 1/4, 261–279.

Einarsson, P. (2008). Plate boundaries, rifts and transforms in Iceland, *Jökull* **58,** no. 12, 35–58.

Einarsson, P. (2010). Mapping of holocene surface ruptures in the South Iceland Seismic Zone, *Jökull* **60,** 121–138.

Einarsson, P. (2014). Mechanisms of Earthquakes in Iceland, in *Encyclopedia of Earthquake Engineering*, M. Beer, I. A. Kougioumtzoglou, E. Patelli, and I. K. Au (Editors), Springer Berlin Heidelberg, Berlin, 1–15, doi: 10.1007/978-3-642-36197-5_298-1.

Einarsson, P., S. Björnsson, G. Foulger, R. Stefánsson, and T. Skaftadóttir (1981). Seismicity pattern in the South Iceland seismic zone, in *Earthquake Prediction: An International Review*, D. W. Simpson and P. G. Richards (Editors), Vol. 4, John Wiley & Sons, 141–151, doi: 10.1029/ME004p0141.

Einarsson, P., Á. R. Hjartardóttir, S. Hreinsdóttir, and P. Imsland (2020). The structure of seismogenic strike-slip faults in the eastern part of the Reykjanes Peninsula Oblique Rift, SW Iceland, *J. Volcanol. Geotherm. Res.* **391,** 106372, doi: 10.1016/j.jvolgeores.2018.04.029.

Field, E. H., T. E. Dawson, K. R. Felzer, A. D. Frankel, V. Gupta, T. H. Jordan, T. Parsons, M. D. Petersen, R. S. Stein, and R. J. Weldon (2009). Uniform California earthquake rupture forecast, version 2 (UCERF 2), *Bull. Seismol. Soc. Am.* **99,** no. 4, 2053–2107.

Frankel, A. D., W. R. Stephenson, D. L. Carver, R. A. Williams, J. K. Odum, and S. Rhea (2007). Seismic hazard maps for Seattle, Washington, incorporating 3D sedimentary basin effects, nonlinear site response, and rupture directivity, *U.S. Geol. Surv. Open-File Rept. 2007-1175*, 77 pp.

Folch, A., C. Abril, M. Afanasiev, G. Amati, M. Bader, R. M. Badia, H. B. Bayraktar, S. Barsotti, R. Basili, and F. Bernardi, *et al.* (2007). The EU Center of Excellence for Exascale in Solid Earth (ChEESE): Implementation, results, and roadmap for the second phase, *Future Gener. Comput. Syst.* **146,** 47–61.

Graves, R., and A. Pitarka (2016). Kinematic ground-motion simulations on rough faults including effects of 3D stochastic velocity perturbations, *Bull. Seismol. Soc. Am.* **106,** no. 5, 2136–2153.

Graves, R., T. H. Jordan, S. Callaghan, E. Deelman, E. Field, G. Juve, C. Kesselman, P. Maechling, G. Mehta, and K. Milner (2011). CyberShake: A physics-based seismic hazard model for southern California, *Pure Appl. Geophys.* **168,** nos. 3/4, 367–381.

Graves, R. W., and A. Pitarka (2010). Broadband ground-motion simulation using a hybrid approach, *Bull. Seismol. Soc. Am.* **100,** no. 5A, 2095–2123.

Grünthal, G., R. Wahlström, and D. Stromeyer (2013). The SHARE European Earthquake Catalogue (SHEEC) for the time period 1900–2006 and its comparison to the European-Mediterranean Earthquake Catalogue (EMEC), *J. Seismol.* **17,** 1339–1344.

Halldórsson, B., and R. Sigbjörnsson (2009). The M_w 6.3 Ölfus earthquake at 15:45 UTC on 29 May 2008 in South Iceland: ICEARRAY strong-motion recordings, *Soil Dynam. Earthq. Eng.* **29,** no. 6, 1073–1083, doi: 10.1016/j.soildyn.2008.12.006.

Halldórsson, B., G. P. Mavroeidis, and A. S. Papageorgiou (2011). Near-fault and far-field strong ground motion simulation for earthquake engineering applications using the specific barrier model, *J. Struct. Eng.* **137,** no. 3, 433–444, doi: 10.1061/(ASCE)ST.1943-541X.0000097.

Halldórsson, B., S. Ólafsson, and R. Sigbjörnsson (2007). A fast and efficient simulation of the far-fault and near-fault earthquake ground motions associated with the June 17 and 21, 2000, earthquakes in South Iceland, *J. Earthq. Eng.* **11,** no. 3, 343–370.

Hjaltadóttir, S. (2009). Use of relatively located microearthquakes to map fault patterns and estimate the thickness of the brittle crust in Southwest Iceland, *Master's Thesis*, Faculty of Earth Sciences, University of Iceland, Reykjavík, Iceland.

Hreinsdóttir, S., T. Árnadóttir, J. Decriem, H. Geirsson, A. Tryggvason, R. A. Bennett, and P. LaFemina (2009). A complex earthquake sequence captured by the continuous GPS network in SW Iceland, *Geophys. Res. Lett.* **36,** no. 12, doi: 10.1029/2009GL038391.

Hreinsdóttir, S., P. Einarsson, and F. Sigmundsson (2001). Crustal deformation at the oblique spreading Reykjanes Peninsula, SW Iceland: GPS measurements from 1993 to 1998, *J. Geophys. Res.* **106,** no. B7, 13,803–13,816, doi: 10.1029/2001JB000428.

Jónasson, K., B. Bessason, Á. Helgadóttir, P. Einarsson, G. B. Guðmundsson, B. Brandsdóttir, K. S. Vogfjörd, and K. Jónsdóttir (2021). A harmonised instrumental earthquake catalogue for

Iceland and the northern Mid-Atlantic Ridge, *Nat. Hazards Earth Syst. Sci.* **21,** no. 7, 2197–2214, doi: 10.5194/nhess-21-2197-2021.

Jordan, T. H., and S. Callaghan (2018). CyberShake models of seismic hazards in southern and central California, *11th National Conference on Earthquake Engineering 2018 (11NCEE) Integrating Science, Engineering, & Policy*, Los Angeles, California, 25–29 June 2018.

Karaca, H. (2021). Generation of synthetic catalog by using Markov chain Monte Carlo simulation and inverse Poisson distribution, *J. Seismol.* **25,** no. 4, 1103–1114.

Kowsari, M., S. Ghasemi, F. Bayat, and B. Halldorsson (2023). A backbone seismic ground motion model for strike-slip earthquakes in Southwest Iceland and its implications for near- and far-field PSHA, *Bull. Earthq. Eng.* **21,** no. 2, 715–738, doi: 10.1007/s10518-022-01556-z.

Kowsari, M., B. Halldorsson, and F. Bayat (2022). Preparation of Finite-fault Earthquake Catalogues Enabling Physics-based PSHA in Southwest Iceland, *Proc. of the 3rd European Conf. on Earthquake and Engineering Seismology (3ECEES)*, Bucharest, Romania, 3863–3870 (No. 8441).

Kowsari, M., B. Halldorsson, B. Hrafnkelsson, J. Þ. Snæbjörnsson, and S. Jónsson (2019). Calibration of ground motion models to Icelandic peak ground acceleration data using Bayesian Markov Chain Monte Carlo simulation, *Bull. Earthq. Eng.* **17,** no. 6, 2841–2870, doi: 10.1007/s10518-019-00569-5.

Kowsari, M., B. Halldorsson, J. Þ. Snæbjörnsson, and S. Jónsson (2021). Effects of different empirical ground motion models on seismic hazard maps for North Iceland, *Soil Dynam. Earthq. Eng.* **148,** 106513, doi: 10.1016/j.soildyn.2020.106513.

Kowsari, M., T. Sonnemann, B. Halldorsson, B. Hrafnkelsson, J. Þ. Snæbjörnsson, and S. Jónsson (2020). Bayesian inference of empirical ground motion models to pseudo-spectral accelerations of South Iceland seismic zone earthquakes based on informative priors, *Soil Dynam. Earthq. Eng.* **132,** 106075, doi: 10.1016/j.soildyn.2020.106075.

Li, B., A.-A. Gabriel, T. Ulrich, C. Abril, and B. Halldorsson (2023). Dynamic rupture models, fault interaction and ground motion simulations for the segmented Húsavík-Flatey Fault Zone, Northern Iceland, *J. Geophys. Res.* **128,** no. 6, e2022JB025886, doi: 10.1029/2022JB025886.

Maechling, P., E. Deelman, L. Zhao, R. Graves, G. Mehta, N. Gupta, J. Mehringer, C. Kesselman, S. Callaghan, D. Okaya, *et al.* (2007). SCEC CyberShake workflows—automating probabilistic seismic hazard analysis calculations, in *Workflows for e-Science: Scientific Workflows for Grids*, I. J. Taylor, E. Deelman, D. B. Gannon, and M. Shields (Editors), Springer, London, 143–163.

Mai, P. M., and G. C. Beroza (2000). Source scaling properties from finite-fault-rupture models, *Bull. Seismol. Soc. Am.* **90,** no. 3, 604–615.

Mai, P. M., and G. C. Beroza (2002). A spatial random field model to characterize complexity in earthquake slip, *J. Geophys. Res.* **107,** no. B11, ESE-10-1–ESE-10-21.

Mavroeidis, G. P., and A. S. Papageorgiou (2003). A mathematical representation of near-fault ground motions, *Bull. Seismol. Soc. Am.* **93,** no. 3, 1099–1131, doi: 10.1785/0120020100.

Mavroeidis, G. P., G. Dong, and A. S. Papageorgiou (2004). Near-fault ground motions, and the response of elastic and inelastic single-degree-of-freedom (SDOF) systems, *Earthq. Eng. Struct. Dynam.* **33,** no. 9, 1023–1049, doi: 10.1002/eqe.391.

Milner, K., B. Shaw, C. Goulet, K. Richards-Dinger, S. Callaghan, T. Jordan, J. Dieterich, and E. Field (2021). Toward physics-based nonergodic PSHA: A prototype fully deterministic seismic hazard model for Southern California, *Bull. Seismol. Soc. Am.* **111,** doi: 10.1785/0120200216.

Morgan, J. P., and M. C. Kleinrock (1991). Transform zone migration: Implications of bookshelf faulting at oceanic and Icelandic propagating ridges, *Tectonics* **10,** no. 5, 920–935, doi: 10.1029/90TC02481.

O'Reilly, O., T.-Y. Yeh, K. B. Olsen, Z. Hu, A. Breuer, D. Roten, and C. A. Goulet (2022). A high-order finite-difference method on staggered curvilinear grids for seismic wave propagation applications with topography, *Bull. Seismol. Soc. Am.* **112,** no. 1, 3–22.

Pagli, C., R. Pedersen, F. Sigmundsson, and K. L. Feigl (2003). Triggered fault slip on June 17, 2000 on the Reykjanes Peninsula, SW Iceland captured by radar interferometry, *Geophys. Res. Lett.* **30,** no. 6, 1273, doi: 10.1029/2002GL015310.

Panzera, F., J. D. Zechar, K. S. Vogfjörd, and D. A. J. Eberhard (2016). A revised earthquake catalogue for South Iceland, *Pure Appl. Geophys.* **173,** no. 1, 97–116, doi: 10.1007/s00024-015-1115-9.

Pedersen, R., S. Jónsson, T. Árnadóttir, F. Sigmundsson, and K. L. Feigl (2003). Fault slip distribution of two June 2000 M_w 6.5 earthquakes in South Iceland estimated from joint inversion of InSAR and GPS measurements, *Earth Planet. Sci. Lett.* **213,** nos. 3/4, 487–502, doi: 10.1016/S0012-821X(03)00302-9.

Rahpeyma, S., B. Halldorsson, B. Hrafnkelsson, and A. Darzi (2023). Frequency-dependent site amplification functions for key geological units in Iceland from a Bayesian hierarchical model for earthquake strong-motions, *Soil Dynam. Earthq. Eng.* **168,** 107823, doi: 10.1016/j.soildyn.2023.107823.

Rojas, O., M. Monterrubio-Velasco, J. E. Rodríguez, S. Callaghan, C. Abril, B. Halldorsson, M. Kowsari, F. Bayat, K. Olsen, and A. Agnes-Gabriel, *et al.* (2022). On the validation of CyberShake in the Southwest Iceland Transform Zone Earthquakes, *Proceedings of the NorthQuake 2022 workshop on Earthquakes in North Iceland*, Húsavík, North Iceland, 19–23 October 2022, p. 57.

Roth, F. (2004). Stress changes modelled for the sequence of strong earthquakes in the South Iceland Seismic Zone Since 1706, in *Geodetic and Geophysical Effects Associated with Seismic and Volcanic Hazards*, J. Fernández (Editor), Pageoph Topical Volumes, Birkhäuser, Basel, 1305–1327.

Rupakhety, R., and R. Sigbjörnsson (2013). Rotation-invariant measures of earthquake response spectra, *Bull. Earthq. Eng.* **11,** no. 6, 1885–1893, doi: 10.1007/s10518-013-9472-1.

Sigbjörnsson, R., G. I. Baldvinsson, and H. Thrainsson (1995). European seismic design practice–research and application, *Proceedings of the 5th SECED Conference*, Chester, United Kingdom, 26–27 October 1995.

Sigbjörnsson, R., S. Ólafsson, R. Rupakhety, B. Halldorsson, P. Acharya, and J. T. Snæbjörnsson (2014). Strong-motion Monitoring and accelerometric recordings in Iceland, *2nd European Conf. on Earthquake and Engineering Seismology (2ECEES)*, Istanbul, Turkey, 24–29 August 2014, Paper No. 2034.

Sigmundsson, F. (2006). Iceland geodynamics, in *Crustal Deformation and Divergent Plate Tectonics*, Springer-Verlag. Berlin, Heidelberg, doi: 10.1007/3-540-37666-6.

Sigmundsson, F., P. Einarsson, R. Bilham, and E. Sturkell (1995). Rift-transform kinematics in South Iceland: Deformation from global

positioning system measurements, 1986 to 1992, *J. Geophys. Res.* **100,** no. B4, 6235–6248, doi: 10.1029/95JB00155.

Silva, F., S. Callaghan, P. J. Maechling, C. A. Goulet, K. R. Milner, R. W. Graves, K. B. Olsen, and T. H. Jordan (2016). Expanding CyberShake physics-based seismic hazard calculations to Central California, *Eos Trans. AGU* (Fall Meet.), Abstracts S31C–2778.

Solnes, J., R. Sigbjörnsson, and J. Eliasson (2004). Probabilistic seismic hazard mapping of Iceland, *13th World Conf. on Earthquake Engineering (13WCEE)*, Vancouver, BC, Canada, 1–6 August 2004, Paper No. 2337.

Stefánsson, R., M. Bonafede, F. Roth, P. Einarsson, Þ. Árnadóttir, and G. B. Guðmundsson (2006). Modelling and parameterizing the Southwest Iceland earthquake release and deformation process, *Rept. VÍ-ES-03 No. 06005*, Icelandic Meteorological Office, 47 pp.

Stefánsson, R., R. Böðvarsson, R. Slunga, P. Einarsson, S. Jakobsdóttir, H. Bungum, S. Gregersen, J. Havskov, J. Hjelme, and H. Korhonen (1993). Earthquake prediction research in the South Iceland seismic zone and the SIL project, *Bull. Seismol. Soc. Am.* **83,** no. 3, 696–716.

Stefansson, R., G. B. Gudmundsson, and P. Halldorsson (2008). Tjörnes fracture zone. New and old seismic evidences for the link between the North Iceland rift zone and the Mid-Atlantic ridge, *Tectonophysics* **447,** nos. 1/4, 117–126, doi: 10.1016/j.tecto.2006.09.019.

Steigerwald, L., P. Einarsson, and Á. R. Hjartardóttir (2020). Fault kinematics at the Hengill Triple Junction, SW-Iceland, derived from surface fracture pattern, *J. Volcanol. Geotherm. Res.* **391,** 106439, doi: 10.1016/j.jvolgeores.2018.08.017.

Stucchi, M., A. Rovida, A. G. Capera, P. Alexandre, T. Camelbeeck, M. B. Demircioglu, P. Gasperini, V. Kouskouna, R. M. W. Musson, and M. Radulian (2013). The SHARE European earthquake catalogue (SHEEC) 1000–1899, *J. Seismol.* **17,** no. 2, 523–544.

Thingbaijam, K. K. S., P. Martin Mai, and K. Goda (2017). New empirical earthquake source-scaling laws, *Bull. Seismol. Soc. Am.* **107,** no. 5, 2225–2246.

Thordarson, T., and A. Hoskuldsson (2002). *Iceland: Classic Geology in Europe*, Terra, United Kingdom.

Tryggvason, E., S. Thoroddsen, and S. Thorarinsson (1958). Report on earthquake risk in Iceland, Vol. 43, Timarit Verkfraedingafelags Islands, 81–97.

Tryggvason, K., E. S. Husebye, and R. Stefánsson (1983). Seismic image of the hypothesized Icelandic hot spot, *Tectonophysics* **100,** no. 1, 97–118, doi: 10.1016/0040-1951(83)90180-4.

Vogfjörd, K. S., G. Nolet, W. J. Morgan, R. M. Allen, R. Slunga, B. H. Bergsson, P. Erlendsson, G. Foulger, S. Jakobsdóttir, and B. Julian (2002). Crustal profiling in Iceland using earthquake source-arrays, *Eos Trans. AGU* (Fall Meet.), Abstracts S61C–1161.

Wells, D. L., and K. J. Coppersmith (1994). New empirical relationships among magnitude, rupture length, rupture width, rupture area, and surface displacement, *Bull. Seismol. Soc. Am.* **84,** no. 4, 974–1002.

Manuscript received 18 April 2024
Published online 10 December 2024